

ANTISYMMETRIC DISTORTED WAVE IMPULSE APPROXIMATION CALCULATIONS FOR COMPOSITE PARTICLE SCATTERING

T. UDAGAWA

Department of Physics, University of Texas, Austin, TX 78712, USA

A. SCHULTE and F. OSTERFELD

Institut für Kernphysik, Kernforschungsanlage Jülich, D-5170 Jülich, West Germany

Received 9 April 1987

(Revised 1 June 1987)

Abstract: Microscopic distorted wave impulse approximation (DWIA) calculations are presented for composite-particle charge exchange scatterings at intermediate energies. A method is developed which permits the exact calculation of the so-called knock-on exchange transition amplitudes. The basic tool used in these calculations is the multipole expansion method which is repeatedly applied to carry out multidimensional integrals. Based on this method a new computer code has been developed which is applied to the $^{90}\text{Zr}(^3\text{He}, t)$ reaction at 600 MeV incident energy. The no-recoil approximation to the knock-on exchange transition amplitude is investigated. The importance of tensor exchange effects for the $(^3\text{He}, t)$ reaction is discussed. A microscopic analysis of the forward angle $^{90}\text{Zr}(^3\text{He}, t)$ spectra is presented using random phase approximation (RPA) wave functions for the description of the nuclear excitation spectrum. We find that the theoretical cross sections calculated with these wave functions describe the data rather well at all scattering angles.

1. Introduction

The (p, n) reaction at intermediate energies ($E \geq 100$ MeV) has been proven to be a very powerful tool for probing spin-isospin modes in nuclei¹⁻⁵). The most prominent of these modes observed in the 0° (p, n) spectra is the giant Gamow-Teller resonance with quantum numbers $L = 0$, $S = 1$, $T = 1$, $J^\pi = 1^+$. The spectra at higher scattering angles ($\theta \geq 0^\circ$) show clear evidence for the collective spin-flip dipole ($L = 1$, $S = 1$, $T = 1$, $J^\pi = 0^-, 1^-, 2^-$) and spin-flip quadrupole ($L = 2$, $S = 1$, $T = 1$, $J^\pi = 1^+, 2^+, 3^+$) resonances. The spin-flip dipole resonance appears in the (p, n) spectra at an excitation energy of $E_x \sim 25$ MeV and at a momentum transfer of $q \sim 0.3\text{--}0.5 \text{ fm}^{-1}$. It has a width Γ of more than 10 MeV. The spin-flip quadrupole resonance is observed as a broad structure at $E_x \sim 35$ MeV in the momentum transfer region $q \sim 0.4\text{--}0.7 \text{ fm}^{-1}$. The resonances are generally rather broad and strongly overlapping. Therefore, one has to decompose the spectra into the various multipoles in order to determine the strength distribution functions of states with different J^π . Recently such a decomposition of the spectra has been successfully carried out for (p, n) and (\vec{p}, \vec{p}') data by several groups⁶⁻¹²). The success of these analyses is based

on the fact that the reaction mechanism operative at intermediate energies is preferentially of direct one-step nature. Therefore, the whole spectra up to high excitation energies ($E_x \leq 50$ MeV) are the result of one-particle-one-hole (1p1h) excitations of the target nucleus.

The decomposition of the spectra into the multipoles is, of course, model dependent. To reduce the model dependence it is helpful to have data of different probes which show a different selectivity for the excitation of the various spin-isospin modes. Such data have, indeed, been accumulated recently for the ($^3\text{He}, t$) reaction at intermediate energies ($E = 200\text{--}400$ MeV/nucleon)^{13,14}. A first analysis¹⁵ of the data shows that this reaction excites the giant spin-flip dipole and giant spin-flip quadrupole resonances much more strongly than the (p, n) reaction. This enhanced excitation of the higher orbital (L) modes is due to the strong surface character of the ($^3\text{He}, t$) reaction.

In order to extract quantitative information from the ($^3\text{He}, t$) data, one has to analyse them in a similar way as the corresponding (p, n) data, i.e. one has to carry out elaborate microscopic antisymmetric nuclear scattering calculations. For that purpose one needs a computer code. For nucleon-nucleus scattering several computer codes such as DWBA70¹⁶), FROST-MARS¹⁷) and TWOFNR¹⁸) are available. These codes treat the inelastic and charge exchange scattering processes fully antisymmetrically. To our knowledge, such a computer code with exact treatment of knock-on exchange does not yet exist for composite particle scattering¹⁹).

In view of the increasing accumulation of intermediate energy ($^3\text{He}, t$) and also (d, 2p) data we decided some time ago to develop a new computer code for composite particle scattering. Recently we have completed the first version, called DCP-1 (Distorted wave impulse approximation code for Composite-Particle scattering)²⁰). With this code a first analysis of 600 MeV $^{90}\text{Zr}(^3\text{He}, t)^{90}\text{Nb}$ data¹³) has already been performed successfully¹⁵).

The primary aim of the present paper is to present the formulation of the DCP-1 calculations. This formulation is given in sect. 2. The basic method that we employ is the multipole expansion method, i.e. we expand the projectile and target transition densities into multipoles. This method turns out to be very suitable for numerical calculations, in particular for the exact calculation of the knock-on exchange effects. This method is different from those employed in previous studies²¹⁻²⁴) where, however, the exchange effect was treated only approximately.

Using the code DCP-1 we investigate the validity of several approximations usually employed in the calculation of the knock-on exchange effects. The most prominent of these is the so-called no-recoil approximation²⁵). In this case one neglects the recoil effects which arise when a nucleon in the projectile and in the target interchange their positions. The no-recoil approximation is in spirit similar to the pseudo-potential approximation²⁶) used in nucleon-nucleus scattering. In sect. 3 we present the results of these studies for the $^{90}\text{Zr}(^3\text{He}, t)$ reaction. In the same section we also discuss the importance of tensor exchange effects and present

a microscopic analysis of forward angle $^{90}\text{Zr}(^3\text{He}, t)$ data¹³⁾ at 600 MeV incident energy. In sect. 4 we summarize the main conclusions of this work.

2. Reaction theory

2.1. DWIA TRANSITION AMPLITUDES

The antisymmetrized DWIA transition amplitude (T) for inelastic and charge exchange scattering, $A(a, b)B$, can be written as a sum of a direct (T^D) and an exchange (T^E) term²⁷⁾

$$T = T^D + T^E, \quad (1)$$

where

$$T^D = \int d\mathbf{r}_a \int dx_1 \int dx_2 \chi_b^{(-)*}(\mathbf{k}_b, \mathbf{r}_a) \langle Bb | V^D(\mathbf{r}) \hat{\rho}_T(x_1, x_1) \hat{\rho}_P(x_2, x_2) | Aa \rangle \chi_a^{(+)}(\mathbf{k}_a, \mathbf{r}_a), \quad (2a)$$

$$T^E = \int d\mathbf{r}_a \int dx_1 \int dx_2 \chi_b^{(-)*}(\mathbf{k}_b, \mathbf{r}_b) \langle Bb | V^E(\mathbf{r}) \hat{\rho}_T(x_1, x'_1) \hat{\rho}_P(x_2, x'_2) | Aa \rangle \chi_a^{(+)}(\mathbf{k}_a, \mathbf{r}_a). \quad (2b)$$

Here, the initial and the final nucleus states of the target are denoted by $|A\rangle$ and $|B\rangle$ and the projectile wave functions by $|a\rangle$ and $|b\rangle$, respectively. As usual, $\chi^{(\pm)}$ are the projectile optical model wave functions. Note that in case of the exchange amplitude, T^E , the channel coordinates \mathbf{r}_a and \mathbf{r}_b are different. They are related by

$$\mathbf{r}_a = \mathbf{r}_b - \frac{\mathbf{r}}{m_a}, \quad (3)$$

where m_a is the mass of the projectile and \mathbf{r} is the distance vector between the two interacting nucleons 1 and 2 of the target and projectile system, respectively (see fig. 1). The difference between \mathbf{r}_a and \mathbf{r}_b arises because of the interchange of the positions of nucleons 1 and 2 in the exchange process. The effective interactions $V^D(\mathbf{r})$ and $V^E(\mathbf{r})$ governing the direct (D) and exchange (E) scatterings are assumed to be local and to contain central and tensor terms. In tensor notation they can be written as

$$V^i = \sum_{k=0,2} \sum_{st} \left(\sum_q S_{kq} Y_{kq}^*(r) \right) V_{stk}^i(r) P_{st} \quad i = D, E, \quad (4)$$

where $S_{00} = 1$ and S_{2q} is the usual (2-rank) tensor operator²⁷⁾. P_{st} is the projection operator projecting onto the spin-isospin subspace with quantum numbers s and t . The corresponding radial parts of the effective interaction are denoted by $V_{stk}^i(r)$ ($i = D, E$).

The quantities $\hat{\rho}_T(x_1, x'_1)$ and $\hat{\rho}_P(x_2, x'_2)$ in eq. (2b) are the non-local density operators for the target (T) and projectile (P) system, respectively. (The corresponding local operators are $\hat{\rho}_T(x_1, x_1)$ and $\hat{\rho}_P(x_2, x_2)$ appearing in T^D , eq. (2a).) These transition operators can be expressed in terms of the nucleon field creation and annihilation operators, $\hat{\Psi}^+(x)$ and $\hat{\Psi}(x)$, as

$$\hat{\rho}_T(x_1, x'_1) = \hat{\Psi}_T^+(x_1) \hat{\Psi}_T(x'_1), \quad (5a)$$

$$\hat{\rho}_P(x_2, x'_2) = \hat{\Psi}_P^+(x_2) \hat{\Psi}_P(x'_2), \quad (5b)$$

where the argument $x_i \equiv (\mathbf{r}_i, \sigma_i, \tau_i)$ stands for the space-, spin-, and isospin-coordinates of nucleon i ($i=1, 2$). The primed coordinates are those after the exchange of nucleons 1 and 2 has taken place. The radial vectors \mathbf{r}'_1 and \mathbf{r}'_2 are measured from the center-of-mass of the target and projectile, respectively. The meaning of the various radial vectors appearing in (5) is schematically shown in fig. 1.

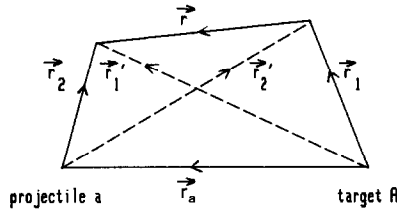


Fig. 1. Coordinates relevant for the scattering of a with A caused by the interaction between nucleons 1 and 2 of the target and projectile system, respectively.

As usual, the field operators $\hat{\Psi}$ are expanded in terms of an appropriate complete set of single-particle wave functions. We use the j -representation for the target operators and the m -representation for the projectile operators, respectively. This leads to

$$\hat{\Psi}_T(x_1) = \sum_{p\nu} \hat{a}_{p\nu} [\phi_p(\mathbf{r}_1) \xi(1)]_{j_p m_p} \eta_\nu(1), \quad (6a)$$

$$\hat{\Psi}_P(x_2) = \sum_{i m \nu} \hat{c}_i \hat{c}_{m\nu} \phi_i(\mathbf{r}_2) \xi_m(2) \eta_\nu(2). \quad (6b)$$

where $\phi(\mathbf{r})$, ξ and η denote the space, spin and isospin parts of the single-particle wave function. For later convenience, we separated the annihilation and creation operators of the projectile system into a space (\hat{c}_i) and spin-isospin ($\hat{c}_{m\nu}$) part.

The target nucleus matrix element of the operator $\hat{\rho}_T(x_1, x'_1)$ (and also $\hat{\rho}_T(x_1, x_1)$) in eq. (2) can then be written as ($\hat{I} = \sqrt{2I+1}$)

$$\begin{aligned} \langle B | \hat{\rho}_T(x_1, x'_1) | A \rangle = & \sum_{l_1 m_1 s_1 m_1 t_1 j_1} \hat{I}_B^{-1} (I_A M_A j_1 m_1 | I_B M_B) \\ & \times (l_1 m_1 s_1 m_1 | j_1 m_1) \rho_{T, l_1 m_1}^{l_1 \nu_1}(\mathbf{r}_1, \mathbf{r}'_1) [\xi(1) \xi(2)^*]_{s_1 m_1} [\eta(1) \tilde{\eta}(2)^*]_{t_1 \nu_1} \end{aligned} \quad (7)$$

with the non-local transition density

$$\rho_{T, l_1 m_{l_1}}^{t_1 \nu_1}(\mathbf{r}_1, \mathbf{r}'_1) \equiv \sum_{ph\nu_p\nu_h} (\frac{1}{2}\nu_p\frac{1}{2}\nu_h | t_1 \nu_1) \hat{f}_p \hat{f}_h \hat{t}_1 \hat{s}_1 \begin{Bmatrix} l_p & \frac{1}{2} & j_p \\ l_h & \frac{1}{2} & j_h \\ l_1 & s_1 & j_1 \end{Bmatrix} \\ \times \langle I_B || [\hat{a}_{p\nu_p}^+ \hat{a}_{h\nu_h}]_{j_i} || I_A \rangle [\phi_p(\mathbf{r}_1) \phi_h(\mathbf{r}'_1)]_{l_1 m_{l_1}} \quad (8a)$$

and the two-nucleon spin wave function

$$[\xi(1)\tilde{\xi}^*(2)]_{s_1 m_1} \equiv \sum_{\nu_1 \nu_2} (\frac{1}{2}\nu_1 \frac{1}{2}\nu_2 | s_1 m_1) \xi_{\nu_1}(1) \xi_{\nu_2}^*(2). \quad (8b)$$

The two-nucleon isospin wave function $[\eta(1)\tilde{\eta}(2)^*]_{t_1 \nu_1}$ in eq. (7) is defined analogously to eq. (8b) (i.e. one replaces ξ by η). The target transition density ρ_T in eq. (8a) consists of a coherent superposition of various particle (p)-hole (h) components. The tilde on top of h indicates that the time reversed state of h is used. $\langle I_B || [\hat{a}_{p\nu_p}^+ \hat{a}_{h\nu_h}]_{j_i} || I_A \rangle$ is the usual spectroscopic amplitude. To the transition density ρ_T we attached the orbital angular momentum quantum numbers ($l_1 m_{l_1}$). We emphasize that ρ depends also on other quantum numbers such as the spin (s_1) and the total angular momentum (j_i), but we omitted them to simplify the notation. Note that l_1 , s_1 and j_i are related by

$$l_1 + s_1 = j_i. \quad (9)$$

We remark that the expression for the expectation value of the diagonal element $\hat{\rho}_T(x_1, x_1)$ can be obtained from eq. (7) by replacing \mathbf{r}'_1 , $\xi(2)$, $\eta(2)$ through \mathbf{r}_1 , $\xi(1)$, $\eta(1)$.

The matrix element of the projectile density operator $\hat{\rho}_P(x_2, x'_2)$ can be written in a similar form as eq. (7):

$$\langle b | \hat{\rho}_P(x_2, x'_2) | a \rangle = \sum \hat{s}_b^{-1} (s_a m_a s_2 m_2 | s_b m_b) \langle b || [\hat{c}^+ \tilde{c}]_{s_2 t_2 \nu_2} || a \rangle \\ \times \rho_P(\mathbf{r}_2, \mathbf{r}'_2) [\xi(2)\tilde{\xi}(1)^*]_{s_2 m_2} [\eta(2)\tilde{\eta}(1)^*]_{t_2 \nu_2}, \quad (10)$$

where

$$\rho_P(\mathbf{r}_2, \mathbf{r}'_2) = \sum_{l_2} \langle b || [\hat{c}_{l_2}^+ \hat{c}_{l_2}]_{00} || a \rangle [\phi_{l_2}(\mathbf{r}_2) \phi_{l_2}(\mathbf{r}'_2)]_{00}. \quad (11)$$

Here we assumed that the space part of the projectile wave function is in a s -state as is the case for scatterings induced by deuteron-, ^3He -, triton- and alpha particles. Projectiles with other internal wave functions can also be treated without any difficulty.

Inserting (6), (7) and (10) into (2), and carrying out the summation over the spin-isospin variables, we obtain the following expression for the transition amplitude T^i ($i = D, E$):

$$T^i = \sum_{j_i s_i l_i m_{l_i}} (-)^{I_A - M_A} (I_A M_A I_B - M_B | j_i - m_{j_i}) (-)^{s_a - m_a} (s_a m_a s_b - m_b | s_i - m_i) \\ \times (s_i m_i j_i m_{j_i} | l_i m_{l_i}) \times \sum_{\substack{k=0,2 \\ l_1, t_1}} \alpha_{t_1 s_1 l_1 k l_i}^{j_i s_i \nu_1} T_{t_1 s_1 l_1 m_{l_i}}^i \quad (12)$$

with the expansion coefficient

$$\alpha_{t_1 s_1 l_1 k l_i}^{j_r s_r \nu_1} = W(s, l, s, l_1; j, k) \hat{s}_r^{-1} \hat{t}_1^{-1} \langle b || [\hat{c}^+ \hat{c}]_{s_r t_1 \nu_1} || a \rangle. \quad (13)$$

The Racah coefficient W involved in eq. (13) describes the recoupling of various angular momenta, while $\langle b || [\hat{c}^+ \hat{c}]_{s_r t_1 \nu_1} || a \rangle$ is the usual spectroscopic amplitude for the projectile spin-isospin wave function. The direct and exchange transition amplitudes are then given by

$$T_{t_1 s_1 l_1 k l_i m_i}^D(\mathbf{k}_b, \mathbf{k}_a) = \int d\mathbf{r}_a \chi_b^{(-)*}(\mathbf{k}_b, \mathbf{r}_a) F_{t_1 s_1 l_1 k l_i m_i}^D(\mathbf{r}_a) \chi_a^{(+)}(\mathbf{k}_a, \mathbf{r}_a), \quad (14a)$$

$$T_{t_1 s_1 l_1 k l_i m_i}^E(\mathbf{k}_b, \mathbf{k}_a) = \int d\mathbf{r}_a \int d\mathbf{r}_b \chi_b^{(-)*}(\mathbf{k}_b, \mathbf{r}_b) F_{t_1 s_1 l_1 k l_i m_i}^E(\mathbf{r}_b, \mathbf{r}_a) \chi_a^{(+)}(\mathbf{k}_a, \mathbf{r}_a), \quad (14b)$$

with the direct and exchange form factors

$$F_{t_1 s_1 l_1 k l_i m_i}^D(\mathbf{r}_a) = \int d\mathbf{r}_1 \int d\mathbf{r}_2 \rho_P^D(\mathbf{r}_2) V_{t_1 s_1 k}^D(\mathbf{r}) [Y_k(\hat{\mathbf{r}}) \rho_{l_1}^D(\mathbf{r}_1)]_{l_i m_i}, \quad (15a)$$

$$F_{t_1 s_1 l_1 k l_i m_i}^E(\mathbf{r}_b, \mathbf{r}_a) = J \int d\mathbf{r}_1 \rho_P^E(\mathbf{r}_2, \mathbf{r}_2') V_{t_1 s_1 k}^E(\mathbf{r}) [Y_k(\hat{\mathbf{r}}) \rho_{l_1}^E(\mathbf{r}_1, \mathbf{r}_1')]_{l_i m_i}. \quad (15b)$$

In eqs. (15a) and (15b) the force components $V_{t_1 s_1 k}^i$ ($i = D, E$) are related to those of eq. (4) by

$$V_{t_1 s_1 k}^i(\mathbf{r}) = \sqrt{4\pi} f_k \hat{t}_1^2 \hat{s}_1^2 \sum_{st} \hat{s}^3 \hat{t}^3 \begin{Bmatrix} \frac{1}{2} & \frac{1}{2} & s \\ \frac{1}{2} & \frac{1}{2} & s \\ s_1 & s_1 & k \end{Bmatrix} \begin{Bmatrix} \frac{1}{2} & \frac{1}{2} & t \\ \frac{1}{2} & \frac{1}{2} & t \\ t_1 & t_1 & 0 \end{Bmatrix} P_i V_{isk}(\mathbf{r}), \quad (16)$$

where $P_D = 1$ and $P_E = (-1)^{s+t+1}$, while $f_0 = 1$ and $f_2 = \sqrt{8}$. The term J in (15b) is the Jacobian associated with the transformation of the integral variable from \mathbf{r}_2 to \mathbf{r}_a .

We now expand the distorted waves $\chi^{(\pm)}$ of eqs. (14) and (15) into partial waves. We choose the coordinate system such that the initial projectile momentum \mathbf{k}_a points along the z -axis:

$$\chi_a^{(+)}(\mathbf{k}_a, \mathbf{r}_a) = \frac{\sqrt{4\pi}}{k_a r_a} \sum_{l_a} i^{l_a} l_a \chi_{l_a}(r_a) Y_{l_a 0}(\hat{\mathbf{r}}_a), \quad (17a)$$

$$\chi_b^{(-)*}(\mathbf{k}_b, \mathbf{r}_b) = \frac{4\pi}{k_b r_b} \sum_{l_b m_{l_b}} i^{-l_b} \chi_{l_b}(r_b) Y_{l_b m_{l_b}}(\hat{\mathbf{r}}_b) Y_{l_b m_{l_b}}^*(\hat{\mathbf{k}}_b). \quad (17b)$$

Using eq. (17) we can rewrite the transition amplitudes in eqs. (14) and (15) according to

$$\begin{aligned} T_{t_1 s_1 l_1 k l_i m_i}^i &= \frac{(4\pi)^{3/2}}{k_a k_b} \sum_{l_a l_b} i^{l_a - l_b + \pi} \hat{l}_a (l_a 0 l_i m_i | l_b m_i) \\ &\quad \times O_{t_1 s_1 l_1 k l_i l_a l_b}^i Y_{l_b m_i}(\hat{\mathbf{k}}_b), \end{aligned} \quad (18)$$

where the $O_{t_1 s_1 l_1 k l_l, l_b l_a}^i$ ($i = D, E$) denote the radial integrals defined by:

$$O_{t_1 s_1 l_1 k l_l, l_b l_a}^D = d_{l_a l_l l_b} \int d\mathbf{r}_a \chi_{l_b}(r_a) f_{t_1 s_1 l_1 k l_l}^D(r_a) \chi_{l_a}(r_a), \quad (19a)$$

$$O_{t_1 s_1 l_1 k l_l, l_b l_a}^E = J \int d\mathbf{r}_b \int d\mathbf{r}_a r_b r_a \chi_{l_b}(r_a) f_{t_1 s_1 l_1 k l_l, l_b l_a}^E(r_b, r_a) \chi_{l_a}(r_a), \quad (19b)$$

with

$$d_{l_a l_l l_b} \equiv \frac{1}{\sqrt{4\pi}} \hat{l}_a \hat{l}_l \hat{l}_b^{-1} (l_a 0 l_l 0 | l_b 0). \quad (19c)$$

The quantities $f_{t_1 s_1 l_1 k l_l}^D(r_a)$ and $f_{t_1 s_1 l_1 k l_l, l_b l_a}^E(r_b, r_a)$ are the radial direct and exchange form factors defined as

$$f_{t_1 s_1 l_1 k l_l}^D(r_a) = i^{-\pi} \int Y_{l_l m_{l_l}}^*(\hat{\mathbf{r}}_a) F_{t_1 s_1 l_1 k l_l m_{l_l}}^D(r_a) d\hat{\mathbf{r}}_a, \quad (20a)$$

$$f_{t_1 s_1 l_1 k l_l, l_b l_a}^E(r_b, r_a) = i^{-\pi} \int [Y_{l_a}(\hat{\mathbf{r}}_b) Y_{l_b}(\hat{\mathbf{r}}_a)]_{l_l m_{l_l}}^* F_{t_1 s_1 l_1 k l_l m_{l_l}}^E(r_b, r_a) d\hat{\mathbf{r}}_a d\hat{\mathbf{r}}_b. \quad (20b)$$

The transition amplitudes of eq. (18) can then be computed once the form factors $f_{t_1 s_1 l_1 k l_l}^D$ and $f_{t_1 s_1 l_1 k l_l, l_b l_a}^E$ are known. Note that the phase factor $i^{-\pi}$ in eq. (20) originates from our insertion of the inverse phase $i\pi$ in eq. (18). We added this phase factor so that the resultant form factor f^i becomes a real quantity. The phase is chosen such that $\pi = 0$ or 1 depending on whether the parity is changed in the reaction or not.

In terms of the transition amplitudes, eq. (14), the differential cross section is given by

$$\frac{d\sigma}{d\Omega} = \frac{\mu_a \mu_b}{(2\pi\hbar^2)^2} \frac{k_b}{k_a} \frac{1}{(2I_A + 1)(2s_a + 1)} \left| \sum_i \sum_{k=0,2} \sum_{l_1, l_l} \alpha_{t_1 s_1 l_1 k l_l}^{j_i s_i \nu_i} T_{t_1 s_1 l_1 l_l m_{l_l}}^i \right|^2 \quad (21)$$

where $\mu_a(\mu_b)$ is the reduced mass in the incident (exit) channel.

2.2. EVALUATION OF FORM FACTORS

2.2.1. Direct form factor. The direct form factor of eq. (20) can be written as an 8-dimensional integral:

$$f_{t_1 s_1 l_1 k l_l}^D(r_a) = i^{-\pi} \int d\hat{\mathbf{r}}_a \int d\mathbf{r}_1 \int d\mathbf{r} Y_{l_l m_{l_l}}^*(\hat{\mathbf{r}}_a) \rho_P^D(\mathbf{r}_2) V_{t_1 s_1 k}(r) [Y_k(\hat{\mathbf{r}}) \rho_{l_1}^D(\mathbf{r}_1)]_{l_l m_{l_l}} \quad (22)$$

where \mathbf{r} is taken to be one of the integration variables. The integration is performed as follows: First we transform $\rho_P^D(\mathbf{r}_2)$ in an explicit function of \mathbf{r} , \mathbf{r}_1 and \mathbf{r}_a . This is

done in two steps: $\rho_P^D(\mathbf{r}_2) \rightarrow \rho_P^D(\mathbf{r}'_2, \mathbf{r}) \rightarrow \rho_P^D(\mathbf{r}_a, \mathbf{r}_1, \mathbf{r})$ using the identities $\mathbf{r}_2 = \mathbf{r}'_2 + \mathbf{r}$ and $\mathbf{r}'_2 = \mathbf{r}_1 - \mathbf{r}_a$ (see fig. 1). In a first step we expand $\rho_P^D(\mathbf{r}_2)$ according to

$$\rho_P^D(\mathbf{r}_2) = \frac{1}{4\pi} \sum_{\lambda_2} \rho_{P,\lambda_2}^D(\mathbf{r}'_2, \mathbf{r}) (-)^{\lambda_2} [Y_{\lambda_2}(\hat{\mathbf{r}}'_2) Y_{\lambda_2}(\hat{\mathbf{r}})]_{00}. \quad (23)$$

and in a second step we expand the resulting function $\rho_{P,\lambda_2}^D(\mathbf{r}'_2, \mathbf{r}) Y_{\lambda_2\mu_2}(\mathbf{r}'_2)$ of (23) once more into

$$\rho_{P,\lambda_2}^D(\mathbf{r}'_2, \mathbf{r}) Y_{\lambda_2\mu_2}(\hat{\mathbf{r}}'_2) = \sqrt{4\pi} \sum_{l'l'} \rho_{P,\lambda_2 l'l'}^D(\mathbf{r}_a, \mathbf{r}_1, \mathbf{r}) [Y_l(\hat{\mathbf{r}}_a) Y_{l'}(\hat{\mathbf{r}}_1)]_{\lambda_2\mu_2}. \quad (24)$$

The phase factor $(-)^{\lambda_2}$ and the constants $(1/4\pi)$ and $\sqrt{4\pi}$ introduced in (23) and (24) are a matter of convenience.

The expansion coefficient $\rho_{P,\lambda_2}^D(\mathbf{r}'_2, \mathbf{r})$ in (23) can be calculated from the usual inverse integral

$$\rho_{P,\lambda_2}^D(\mathbf{r}'_2, \mathbf{r}) = \sqrt{16\pi^3} \int \rho_P^D(\mathbf{r}'_2, \mathbf{r}, \mu) Y_{20}(\theta, 0) d\mu \quad (\mu = \mathbf{r} \cdot \mathbf{r}'_2). \quad (25)$$

The function $\rho_{P,\lambda_2 l'l'}^D(\mathbf{r}_a, \mathbf{r}_1, \mathbf{r})$ in (24) may also be calculated from a similar inverse integral, which, however, is not as simple as the one in (25), since the original function is not a scalar function. Nevertheless, it is possible to reduce the integral to a one-dimensional form since the integrand depends only on the variables $\mu = \cos \theta = \mathbf{r}_1 \cdot \mathbf{r}_a$, \mathbf{r}_1 and \mathbf{r}_a . Choosing the z-axis along the vector \mathbf{r}_a (see fig. 2) one can write $\rho_{P,\lambda_2 l'l'}^D$ in the following way:

$$\begin{aligned} \rho_{P,\lambda_2 l'l'}^D(\mathbf{r}_a, \mathbf{r}_1, \mathbf{r}) &= \frac{2\pi}{2\lambda_2 + 1} \sum_m \hat{l} \langle l 0 l' m | \lambda_2 m \rangle \\ &\times \int \rho_{P,\lambda_2 l'l'}^D(\mathbf{r}_a, \mathbf{r}_1, \mu, \mathbf{r}) Y_{\lambda_2 m}(\theta'_2, 0) Y_{l' m}^*(\theta, 0) d\mu, \\ &(\mu \equiv \cos \theta = \hat{\mathbf{r}}_a \cdot \hat{\mathbf{r}}_1 \quad \text{and} \quad \mu' \equiv \cos \theta' = \hat{\mathbf{r}}_a \cdot \hat{\mathbf{r}}'_2). \end{aligned} \quad (26)$$

Inserting (23) together with (24) and (26) into (22) and carrying out the integrals

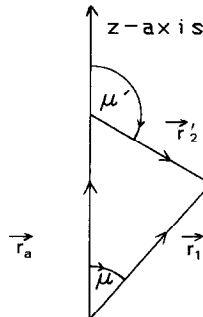


Fig. 2. Choice of coordinate system for the projectile density expansion. The z-axis points along the vector \mathbf{r}_a .

over the angle variables, we obtain as a final expression for the direct form factor

$$f_{t_1 l_1 s_1 k l_l}^D(r_a) = (-)^{l_l} \hat{l}_l^{-1} \int d\mathbf{r} r^2 V_{t_1 s_1 k}^D(r) \int r_1^2 d\mathbf{r}_1 \rho_{P, k l_l}^D(r_a, \mathbf{r}_1, r) \rho_{T, l_l}^D(r_1). \quad (27)$$

Note that f^D is given by $\rho_{P, \lambda_2 l' l}^D$ with $\lambda_2 = k$, $l = l_l$ and $l' = l_1$. This means that for a given set of $t_1 l_1 s_1 k l_l$ we have to calculate only one term in the expansion of (25).

2.2.2. Exchange form factors. Inserting (15b) into (20b), one can write the exchange form factor as

$$f_{f_1 s_1 l_1 k l_l l_b}^E(r_b, r_a) = J l^{-\pi} \int d\hat{\mathbf{r}}_a \int d\hat{\mathbf{r}}_b \int d\mathbf{r}_1 [Y_{l_b}(\hat{\mathbf{r}}_a) Y_{l_b}(\hat{\mathbf{r}}_b)]_{l_l m_l} \times \rho_P^E(\mathbf{r}_2, \mathbf{r}'_2) V_{t_1 s_1 k}^E(r) [Y_k(\hat{\mathbf{r}}) \rho_{T, l_1}^E(\mathbf{r}_1, \mathbf{r}'_1)]_{l_l m_l}. \quad (28)$$

In this case we have to carry out a 7-dimensional integral. We do this in more or less a similar manner as we did before for the direct form factor; i.e. we repeatedly use the multipole expansion method.

We proceed as follows; We first define $c_{t_1 s_1 l_1 m_l}^k(\mathbf{r}_b, \mathbf{r})$ by

$$c_{t_1 s_1 l_1 m_l}^k(\mathbf{r}_b, \mathbf{r}) = \sqrt{1/4\pi} r^{-k} V_{t_1 s_1 k}^E(r) \int d\mathbf{r}_1 \rho_P^E(\mathbf{r}_2, \mathbf{r}'_2) \rho_{T, l_1 m_l}^E(\mathbf{r}_1, \mathbf{r}'_1), \quad (29)$$

and perform the integral over \mathbf{r}_1 . For this purpose, we expand the two non-local densities ρ_P^E and ρ_T^E as follows:

$$\rho_P^E(\mathbf{r}_2, \mathbf{r}'_2) = \sum_{\lambda_2} \rho_{P, \lambda_2}^E(r'_2, r) (-)^{\lambda_2} [Y_{\lambda_2}(\hat{\mathbf{r}}'_2) Y_{\lambda_2}(\hat{\mathbf{r}})]_{00}, \quad (30a)$$

$$\rho_{T, l_1 m_l}^E(\mathbf{r}_1, \mathbf{r}'_1) = \sum_{\lambda_1 l_p} \rho_{T, l_1 l_p \lambda_1}^E(r_1, r) [Y_{l_p}(\hat{\mathbf{r}}_1) Y_{\lambda_1}(\hat{\mathbf{r}})]_{l_1 m_l}. \quad (30b)$$

The expansion coefficients may be calculated by following the same procedure as described in the previous subsection. The final results for $\rho_{P, \lambda_2}^E(r'_2, r)$ and $\rho_{T, l_1 l_p \lambda_1}^E(r_1, r)$ are given by

$$\rho_{P, \lambda_2}^E(r'_2, r) = \sum_{l_2 l'_2} \hat{l}_2 \hat{l}'_2 \omega_{l_2}(r'_2) (l'_2 0 \lambda_2 0 | l_2 0) \times \frac{2\pi}{2l_2 + 1} \sum_{m_2} \hat{l}'_2 (l'_2 0 \lambda_2 m_2 | l_2 m_2) \int \omega_{l_2}(r_2) Y_{\lambda_2 m_2}(\theta, 0) Y_{\lambda_2 m_2}(\theta', 0) d\mu, \quad (31a)$$

$$(\mu = \cos \theta = \mathbf{r}_2 \cdot \mathbf{r}'_2 \quad \text{and} \quad \cos \theta' = \mathbf{r}'_2 \cdot \mathbf{r})$$

$$\rho_{T, l_1 l \lambda_1}^E(r_1, r) = \sum_{p h l_h} i^{l_p + l_h - \pi} \hat{j}_p \hat{j}_h \hat{l}_1 \hat{s}_1 \begin{Bmatrix} l_p & \frac{1}{2} & j_p \\ l_h & \frac{1}{2} & j_h \\ l_1 & s_1 & j_i \end{Bmatrix} \langle I_B \| [\hat{a}_{p\nu_p}^+ \hat{a}_{h\nu_h}]_{j_i} \| I_A \rangle$$

$$\times (-)^{l_h} \hat{l}_h \hat{l}'_h \hat{l}'_p (l'_p 0 l'_h 0 | l_p 0) W(l'_p l'_h l_h; l_p \lambda_1) R_{l_p}(r_1)$$

$$\times \frac{2\pi}{2l_h + 1} \sum_{m_1} \hat{l}'_h (l'_h 0 \lambda_1 m_1 | l_h m_1) \int R_{l_h}(r'_1) Y_{l_h m_1}(\theta, 0) Y_{\lambda_1 m_1}^*(\theta', 0) d\mu', \quad (31b)$$

$$(\mu = \cos \theta = \hat{\mathbf{r}}'_1 \cdot \hat{\mathbf{r}}'_1 \quad \text{and} \quad \mu' \equiv \cos \theta' = \hat{\mathbf{r}}_1 \cdot \hat{\mathbf{r}}).$$

In (31b), $R(r)$ is the radial part of the single-particle wave function $\phi_p(\mathbf{r})$.

We further expand $\rho_{P,\lambda_2}^E(r'_2, r) Y_{\lambda_2\mu_2}(\hat{\mathbf{r}}'_2)$ in (31a) similarly to (24)

$$\rho_{P,\lambda_2}^E(r'_2, r) Y_{\lambda_2\mu_2}(r'_2) = \sum_{ll'} \rho_{P,\lambda_2 ll'}^E(r_b, r_1, r) \sqrt{4\pi} [Y_l(\hat{\mathbf{r}}_b) Y_{l'}(\hat{\mathbf{r}}_1)]_{\lambda_2\mu_2}. \quad (32)$$

Since the expansion coefficient can be written in exactly the same way as stated before in (26), we do not repeat it here.

Using (30), the angular part of the integration in (29) can be carried out analytically, and the resultant $c_{l_1 s_1 l_1 m_{l_1}}^k$ is obtained as a function of \mathbf{r}_b and \mathbf{r} :

$$c_{l_1 s_1 l_1 m_{l_1}}^k(\mathbf{r}_b, \mathbf{r}) = \sum_{l\lambda} i^\pi G_{l_1 s_1 l_1 l\lambda}^k(r_b, r) [Y_l(\hat{\mathbf{r}}_b) Y_\lambda(\hat{\mathbf{r}})]_{l_1 m_{l_1}}, \quad (33a)$$

$$\begin{aligned} G_{l_1 s_1 l_1 l\lambda}^k(r_b, r) &= \sqrt{1/4\pi} r^{-k} V_{l_1 s_1 k}^E(r) \sum_{\lambda_1 \lambda_2 l'_p} (-)^{l'_p} \hat{\lambda}_1 \hat{\lambda}_2 (\lambda_1 0 \lambda_2 0 | \lambda 0) \\ &\times W(\lambda_1 \lambda_2 l_1 l; \lambda l'_p) \int r_1^2 d\mathbf{r}_1 \rho_{T, l_1 l'_p \lambda_1}^E(r_b, r) \rho_{P, \lambda_2 l'_p}^E(r_b, r_1, r). \end{aligned} \quad (33b)$$

We are now ready to transform $c_{l_1 s_1 l_1 m_{l_1}}^k(\mathbf{r}_b, \mathbf{r})$ to a function of \mathbf{r}_b and \mathbf{r}_a by using eq. (3) with the result

$$c_{l_1 s_1 l_1 m_{l_1}}^k(\mathbf{r}_b, \mathbf{r}_a) = \sum_{l'_b l'_a} c_{l'_b l'_a}^{l_1 s_1 l_1 k}(\mathbf{r}_b, \mathbf{r}_a) [Y_{l'_a}(\hat{\mathbf{r}}_a) Y_{l'_b}(\hat{\mathbf{r}}_b)]_{l_1 m_{l_1}}, \quad (34)$$

where the expansion coefficient is calculated as

$$\begin{aligned} c_{l'_b l'_a}^{l_1 s_1 l_1 k}(\mathbf{r}_b, \mathbf{r}_a) &= \frac{2\pi}{2l_t + 1} \sum_{m_{l_t}} \hat{l}'_b (l'_a m_{l_t} l'_b 0 | l m_{l_t}) \sum_{l\lambda} \hat{l} (l 0 \lambda m_{l_t} | l_t m_{l_t}) \\ &\times \int d\mu G_{l_1 s_1 l_1 l\lambda}(r_b, r) Y_{\lambda m_{l_t}}(\theta', \pi) Y_{l'_a m_{l_t}}^*(\theta, 0), \end{aligned} \quad (35)$$

$$(\mu = \cos \theta = \hat{\mathbf{r}}_b \cdot \hat{\mathbf{r}}'_a \quad \text{and} \quad \cos \theta' = \hat{\mathbf{r}}_b \cdot \hat{\mathbf{r}}).$$

Using this and also the well known addition theorem for the vector spherical harmonics, which we apply to $r^k Y_{kq}(r)$ in (28), we obtain the following final expression for f^E ,

$$\begin{aligned} f_{l_1 s_1 l_1 k l_t, l_b l_a}^E(\mathbf{r}_b, \mathbf{r}_a) &= 4\pi \sum_{\lambda_a \lambda_b l'_a l'_b} \left[\frac{(2k+1)!}{(2\lambda_1+1)!(2\lambda_b+1)!} \right]^{1/2} \delta_{\lambda_a + \lambda_b, k} \\ &\times (r_b)^{\lambda_b} (-r_a)^{\lambda_a} \hat{k} \hat{l}_1 \hat{l}_a \hat{l}_b \begin{Bmatrix} l'_a & \lambda_a & l_a \\ l'_b & \lambda_b & l_b \\ l_1 & k & l_t \end{Bmatrix} d_{l'_a \lambda_a l_a} d_{l'_b \lambda_b l_b} \\ &\times c_{l'_b l'_a}^{l_1 s_1 l_1 k}(\mathbf{r}_b, \mathbf{r}_a). \end{aligned} \quad (36)$$

2.3. THE LIMITING CASE OF NUCLEON-NUCLEUS SCATTERING

The formulae derived in the previous subsections for composite particle scattering can be applied to nucleon-nucleus scattering if a certain limit is taken for the projectile transition density. In fact, if we adopt the following limits

$$\rho_P^D(\mathbf{r}_2) \rightarrow \delta(\mathbf{r}_2), \quad (37a)$$

$$\rho_P^E(\mathbf{r}_2, \mathbf{r}_2') \rightarrow \delta(\mathbf{r}_2). \quad (37b)$$

the form factors given by eqs. (14b) and (15b) are reduced to the corresponding form factors for nucleon-nucleus scattering:

$$F^D(\mathbf{r}_a) = \int d\mathbf{r}_1 V_{t_1 s_1 k}^D(r) [Y_k(\hat{\mathbf{r}}) \rho_{T, l_1}(\mathbf{r}_1)]_{l, m_l}, \quad (38a)$$

$$F^E(\mathbf{r}_b, \mathbf{r}_a) = V_{t_1 s_1 k}^E(r) [Y_k(\hat{\mathbf{r}}) \rho_{T, \lambda_1}^E(\mathbf{r}_b - \mathbf{r}, \mathbf{r}_b)]_{l, m_l}. \quad (38b)$$

Taking the limits of eqs. (37a) and (37b) is equivalent to make the following replacements in eqs. (24) and (30a):

$$\rho_{P, \lambda_2}^D(r_2', r) \rightarrow \lambda_2 \delta(r_2' - r) / r^2, \quad (39a)$$

$$\rho_{P, \lambda_2}^E(r_2', r) \rightarrow \lambda_2 (-)^{\lambda_2} \delta(r_2' - r) / r^2. \quad (39b)$$

From eqs. (27) and (36) we can then calculate the form factors for nucleon-nucleus scattering.

2.4. DISCUSSION

Based on the formalism presented in the preceding subsections, we have developed the computer code DCP-1 (DWIA calculations for Composite-Particle-scatterings)²⁰⁾. The code was first applied to the analysis of $^{90}\text{Zr}(^3\text{He}, t)^{90}\text{Nb}$ data at $E = 600$ MeV. First results of this analysis have already been reported¹⁵⁾. At present, we are extending the analysis to other reactions like $(d, 2p)$ and $(^6\text{Li}, ^6\text{He})$. The results of these studies will be published elsewhere²⁸⁾.

In the following, we briefly discuss the efficiency of the method presented here. As described in the preceding subsections, we expand the projectile and target transition densities into multipoles. The efficiency of this approach is then determined by the rapidity of the convergence of the expansion. We have found that the convergence is reasonably fast and accurate. To obtain an accuracy of 1%, it is sufficient to retain only the lowest order expansion term for the projectile density, i.e. only the $\lambda_2 = 0$ term, and the first three or four terms (i.e. $\lambda = \lambda_1 \leq 3$) for the target density. Because of this rapid convergence, the present method enables us to carry out even the complicated knock-on exchange amplitude calculations within a reasonable computation time. We remark that both central and tensor forces can be included in the calculations.

We also mention that the present method can be applied to any form of the effective interaction. This means that the radial dependence of the effective interaction has *not* to be of Yukawa or Gauss type as is usually required in the computer codes^{16–18)} for nucleon–nucleus scattering. Therefore the present code is rather general with respect to the choice of the effective projectile nucleon–target nucleon interaction.

3. Numerical calculations

As was already remarked in the introduction there exists no exact evaluation of the knock-on exchange transition amplitude for composite particle scattering. So far all calculations have been performed in the so-called pseudo-potential approximation. On the other hand, it is known that in case of nucleon–nucleus scattering the accuracy of the pseudo-potential varies considerably with the projectile energy, the target mass and with the final nucleus spin^{26,29)}. For this reason we have examined the accuracy of this approximation using the code DCP-1. We have also examined the tensor exchange effects, which have been neglected in the previous nucleon–nucleus scattering calculations^{10,11)}. In the present section, we discuss the results of such studies.

3.1. NO-RECOIL APPROXIMATION

The no-recoil approximation was originally invented to simplify the cross section calculations for heavy ion induced one and two nucleon transfer reactions^{22,25)}. The essence of the approximation is to ignore the recoil momentum which the target receives in the transfer process. In the same spirit we neglect here the recoil momenta which projectile and target pick up in the knock-on exchange process.

Formally this approximation is obtained by replacing $\chi_a^{(+)}(\mathbf{k}_a, \mathbf{r}_a)$ in (15a) through $\chi_a^{(+)}(\mathbf{k}_a, \mathbf{r}_b)$, i.e. ignoring the difference between the vectors \mathbf{r}_a and \mathbf{r}_b . Then the exchange transition amplitude in eq. (15) is simplified to

$$T_{t_1 s_1 l_1 k l m_l}^E(\mathbf{k}_b, \mathbf{k}_a) = \int d\mathbf{r}_b \chi_b^{(-)*}(\mathbf{k}_b, \mathbf{r}_b) F_{t_1 s_1 l_1 k l m_l}^{\text{NR}}(\mathbf{r}_b) \chi_a^{(+)}(\mathbf{k}_a, \mathbf{r}_b), \quad (40a)$$

$$F_{t_1 s_1 l_1 k l m_l}^{\text{NR}}(\mathbf{r}_b) = \int d\mathbf{r} \int d\mathbf{r}_1 \rho_p^E(\mathbf{r}_2, \mathbf{r}_2') V_{t_1 s_1 k}^E(r) [Y_k(\hat{\mathbf{r}}) \rho_{T, l_1}^E(\mathbf{r}_1, \mathbf{r}_1')]_{l m_l}. \quad (40b)$$

Eq. (40) has a similar structure as eq. (14) which defines the direct transition amplitude. Therefore, by introducing the no-recoil approximation, we can evaluate the exchange transition amplitude in a similar manner as the direct one. The only modification we have to make is to replace the direct form factor $f_{t_1 s_1 l_1 k l}^D(\mathbf{r}_b)$ in (19a) by the no-recoil form factor $f_{t_1 s_1 l_1 k l}^{\text{NR}}(\mathbf{r}_b)$ which in terms of the quantity $G_{t_1 s_1 l_1 l k}^k(\mathbf{r}_b, \mathbf{r})$

of eq. (33) is given by

$$f_{l_1 s_1 l_1 k l_1}^{\text{NR}}(r_b) = \sqrt{4\pi} (-)^{l_1+k-l_1} \hat{l}_1 \hat{l}_1^{-1} \int dr r^{2+k} G_{l_1 s_1 l_1 l_1}^k(r_b, r). \quad (41)$$

The question arises how accurate the no-recoil approximation really is. In order to test this we performed differential cross section calculations at 600 MeV incident energies for various $^{90}\text{Zr}(^3\text{He}, t)^{90}\text{Nb}$ reactions leading to different final nucleus states J^π . The calculations were carried out within the distorted wave impulse approximation (DWIA) using the free nucleon-nucleon t -matrix parametrized by Love and Franey³⁰⁾ for the effective projectile nucleon-target nucleon interaction. The optical potentials used for the evaluation of the distorted waves in the incident and exit channels were generated from the 200 MeV proton optical potentials of ref.³⁴⁾ by following the single folding procedure. The experimental projectile ground state density distribution was taken from ref.³²⁾ as well as the magnetic density distribution which is needed in the charge exchange form factor calculations. The wave functions for the nuclear excited states were calculated within the random phase approximation (RPA). The RPA model space included all $4\hbar\omega$ particle-hole (ph) excitations. The residual ph-interaction was taken from ref.⁹⁾.

The cross sections calculated either in exact finite range (EFR) or in the no-recoil approximation (NR) are shown in figs. 3 and 4 by full and dashed lines, respectively. As can be seen, the calculated NR cross sections (σ^{NR}) are systematically larger than the exact ones (σ^{EX}). Since in case of the Love-Franey interaction³⁰⁾ the direct and exchange transition amplitudes interfere destructively, the above result, $\sigma^{\text{NR}} \geq \sigma^{\text{EX}}$ implies that the NR approximation leads to an underestimate of the exchange effects. From the results in figs. 3 and 4 it is clear that the accuracy of the NR approximation is state dependent. In some cases it works rather well (30% accuracy) while in others not. A particularly large deviation occurs for the 0^- , $E_x = 27.9$ MeV transition shown in fig. 3. In this case the NR result differs from the exact one by about a factor of 5 at high momentum transfers.

3.2. TENSOR EXCHANGE EFFECTS

In charge exchange reactions both the central and tensor force components of the nucleon-nucleon- t -matrix contribute to the magnitude and shape of the differential cross sections. Since the tensor knock-on exchange effect is difficult to calculate it is often neglected in the cross section calculations^{10,11)}. Here we check the accuracy of this approximation for the $(^3\text{He}, t)$ reaction.

In figs. 5 and 6 we present the results of these studies for different final nucleus states J^π . The dashed and long-short-short-dashed curves represent the differential cross sections of the central and tensor forces alone, while the full and dotted curves denote the complete calculations with and without tensor exchange. To estimate the tensor exchange effect one has to compare the full curves with the dotted ones.

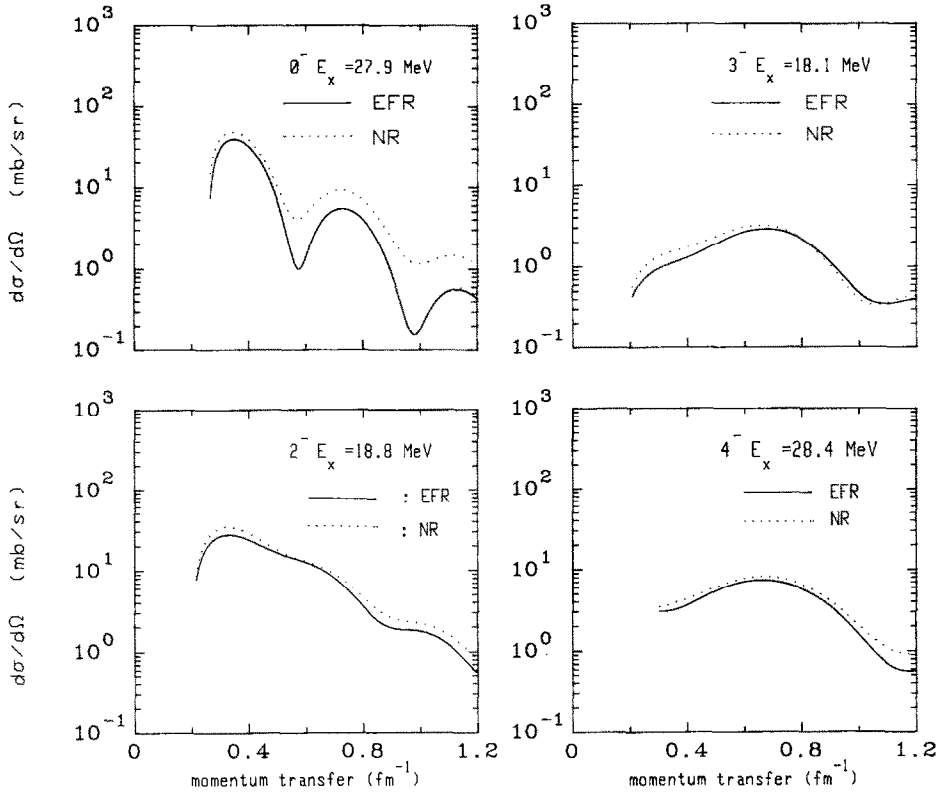


Fig. 3. Calculated differential cross sections for the $^{90}\text{Zr}(^3\text{He}, t)^{90}\text{Nb}$ reaction at 600 MeV incident energy leading to the collective $J^\pi = 0^-, 2^-, 3^-$ and 4^- final nucleus states. The full lines denote the cross sections where the knock-on exchange amplitude has been calculated in exact finite range (EFR) while the dotted curves denote the cross sections calculated in the no-recoil approximation (NR).

Apparently the tensor exchange effect is small and can be safely neglected in the calculations.

3.3. THE EXCITATION OF HIGHER MULTIPOLE STATES IN THE $(^3\text{He}, t)$ REACTION

The $(^3\text{He}, t)$ reaction probes the nuclear structure in a different way than the (p, n) reaction. To show this we studied the angular distributions to the collective $1\hbar\omega$ and $2\hbar\omega$ final nuclear states. In the left panel of fig. 7 we show the results for the collective $1\hbar\omega$ 0^- , 1^- and 2^- transitions. The full lines represent the $(^3\text{He}, t)$ cross sections while the dotted curves represent the (p, n) cross sections. Note that the (p, n) results are smaller by a factor 2–4 in forward direction than the $(^3\text{He}, t)$ results. In a plane wave limit one would expect a factor of 9 simply due to kinematical reasons. The reduction of this factor from 9 to 2–4 is a consequence of the stronger absorption suffered by the ^3He - and t -projectiles as compared to proton and neutron

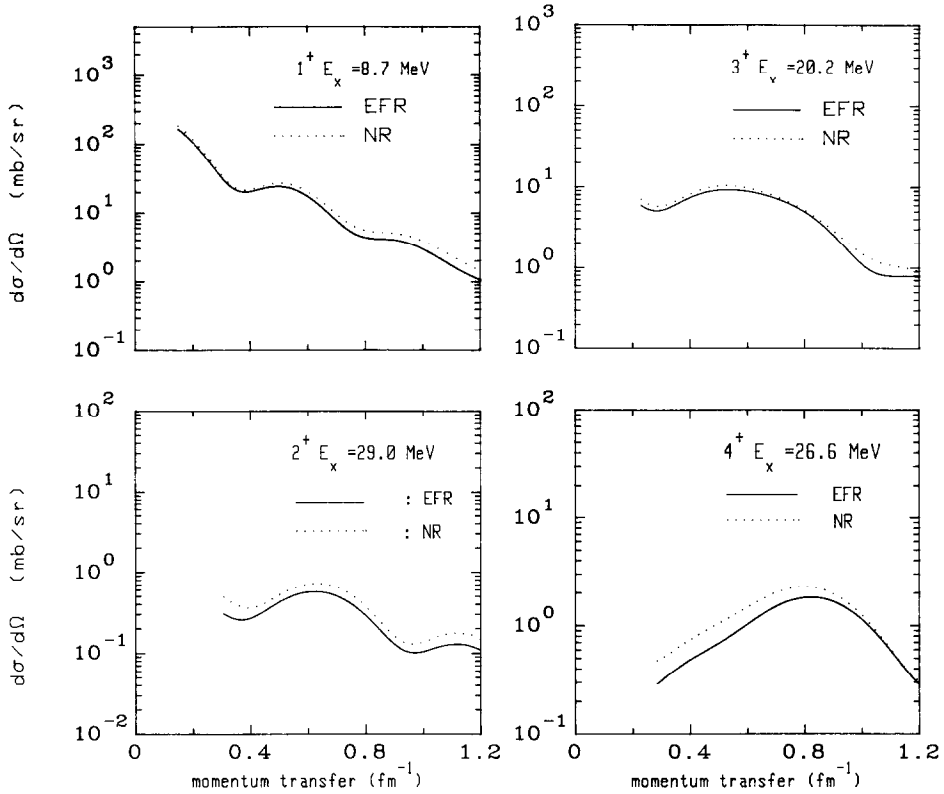


Fig. 4. Same as in fig. 3 but now for the $J^\pi = 1^+, 2^+, 3^+$ and 4^+ final nucleus states.

projectiles. In the right panel of fig. 7 we show the cross sections to the collective $2\hbar\omega$, $J^\pi = 1^+, 2^+$ and 3^+ states. Now the ratios between the low momentum transfer ($^3\text{He}, t$) and the corresponding (p, n) cross sections are almost 10. The reason for this enhancement is found in the strong surface character of the ($^3\text{He}, t$) reaction. In order to prove this we studied the transition to the $2\hbar\omega$, $J^\pi = 1^+ E_x = 29.8 \text{ MeV}$ state in more detail. In the upper part of fig. 8 we show the direct RPA transition density to this state. We see that this density has a node near the nuclear surface. Because of the stronger absorption of the ($^3\text{He}, t$) probe in comparison to the (p, n) probe this node acts in both reactions very differently.

To demonstrate this we give the differential ($^3\text{He}, t$) and (p, n) cross sections to this state obtained by introducing a lower radial cutoff in the nuclear transition form factor. Note that the (p, n) cross section is very sensitive to this cutoff, especially if the cutoff radius reaches the nuclear surface. Then the (p, n) cross section suddenly rises and has a similar shape as the ($^3\text{He}, t$) cross section. The latter, however, is rather insensitive to a cutoff smaller than 4 fm. This indicates that the ($^3\text{He}, t$) reaction is a surface reaction dominantly taking place in the outer region of the

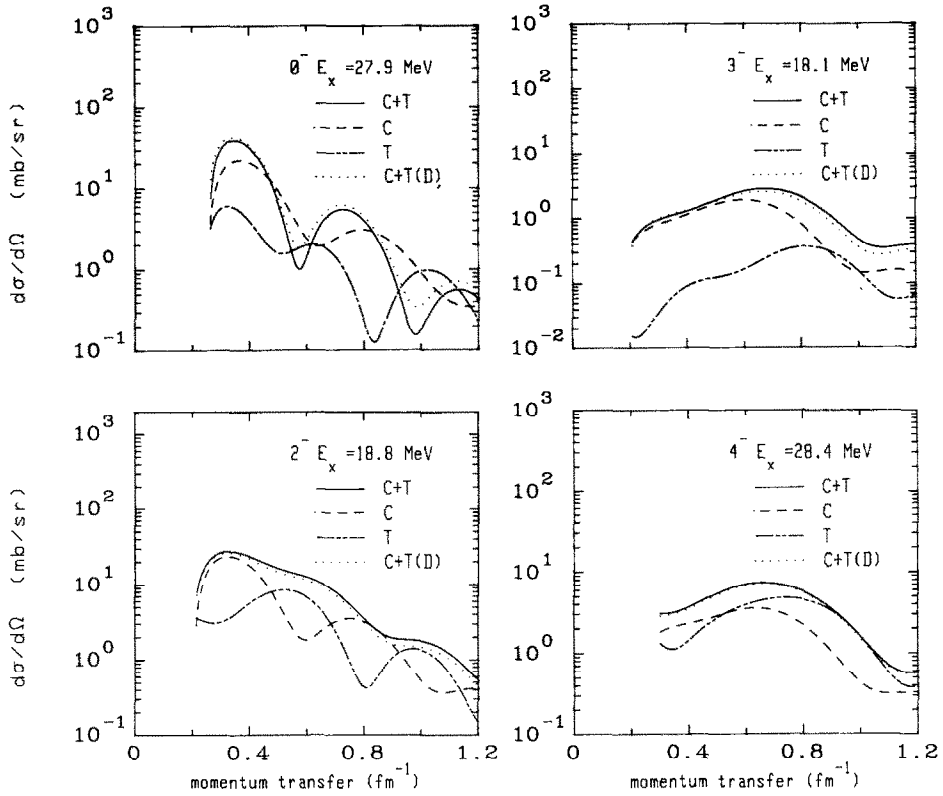


Fig. 5. Calculated differential cross sections for the $^{90}\text{Zr}(^3\text{He}, t)^{90}\text{Nb}$ reaction at 600 MeV incident energy leading to the collective $J^\pi = 0^-, 2^-, 3^-$ and 4^- final nucleus states. Cross sections corresponding to the following contributions are shown: charge exchange with central (C) force (short dashed curve) and with tensor (T) force (long-short-short-dashed curve), charge exchange with central plus tensor forces but once with (full curve) and once without (dotted curve) the inclusion of the tensor exchange amplitudes.

nucleus, i.e. outside 4 fm. In contrast to that the proton also probes the interior of the nucleus. Therefore the internal and external components of the nuclear transition density can cancel making the resulting (p, n) cross section small.

3.4. ANALYSIS OF $^{90}\text{Zr}(^3\text{He}, t)$ SPECTRA

After the study of the various properties of the $(^3\text{He}, t)$ reaction we now present a microscopic analysis of the complete forward angle $^{90}\text{Zr}(^3\text{He}, t)$ spectra at 600 MeV incident energy. A similar analysis was published already previously by us¹⁵⁾ but at that time we considered a smaller RPA model space (all $\leq 2\hbar\omega$ particle-hole excitations were included) than in the present calculations. Now we extended the RPA model space to all $\leq 4\hbar\omega$ excitations. This permits us to test the convergence properties of the cross section calculations. The residual ph-interaction was again taken from ref. 9). All transitions with multipolarities $J^\pi \leq 5^-$ were taken into account.

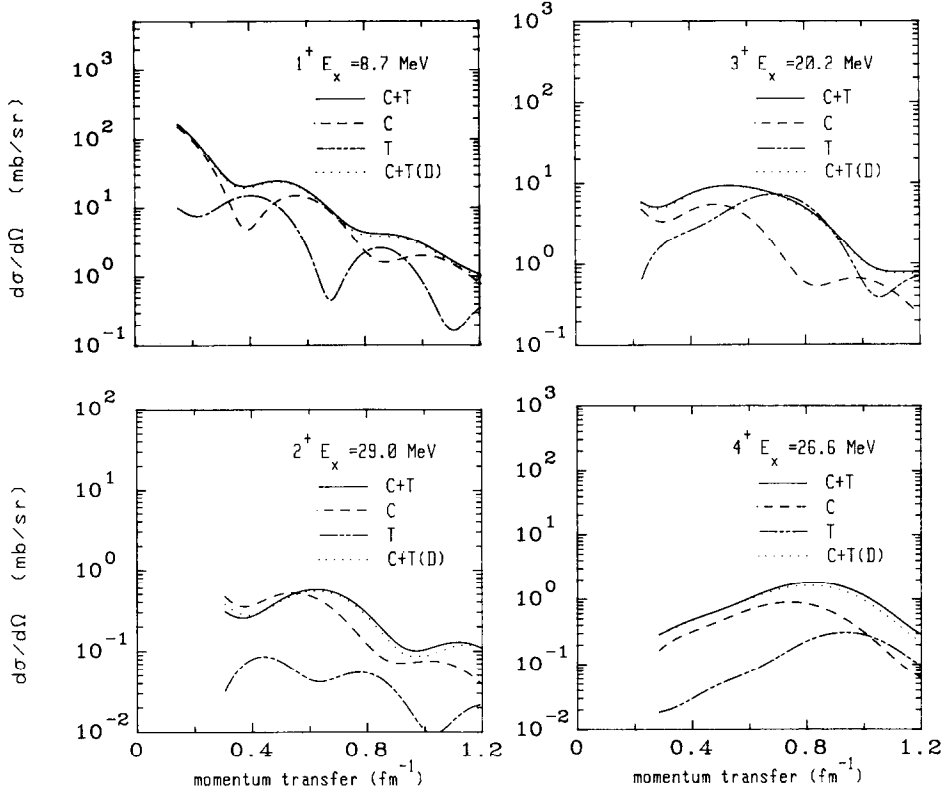


Fig. 6. Same as in fig. 5 but now for $J^\pi = 1^+, 2^+, 3^+$ and 4^+ final nucleus states.

With our newly developed computer code DCP-1 we first calculated for each RPA-final state n the differential cross section $d\sigma_n/d\Omega$. We then obtained the continuous spectrum, $d^2\sigma/d\Omega dE$, by folding the cross sections $d\sigma_n/d\Omega$ into an asymmetric Breit-Wigner function

$$\frac{d^2\sigma}{d\Omega dE} = \frac{2}{\pi} \sum_n (\Gamma_{n,r} + \Gamma_{n,l}) \left[\frac{\Gamma_{n,l}^2 \theta(E_n + \Delta E_J - E)}{(E - E_n - \Delta E_J)^2 + \Gamma_{n,l}^2} + \frac{\Gamma_{n,r}^2 \theta(E - E_n - \Delta E_J)}{(E - E_n - \Delta E_J)^2 + \Gamma_{n,r}^2} \right] \times d\sigma_n/d\Omega.$$

Here, E_n and Γ_n denote the excitation energy and width of the RPA-state n , respectively, $\theta(E)$ is the usual step function and ΔE_J is a free parameter which allows us to shift the centroid energy of the RPA-strength distribution for a given spin J^π by that amount. To fix the right and left widths $\Gamma_{n,r}$ and $\Gamma_{n,l}$ we set the average width $\frac{1}{2}(\Gamma_{n,r} + \Gamma_{n,l})$ equal to twice the imaginary part of the empirical nucleon-nucleus optical potential, i.e.

$$\frac{1}{2}(\Gamma_{n,r} + \Gamma_{n,l}) = 2W(E_n - \varepsilon_F, R_w).$$

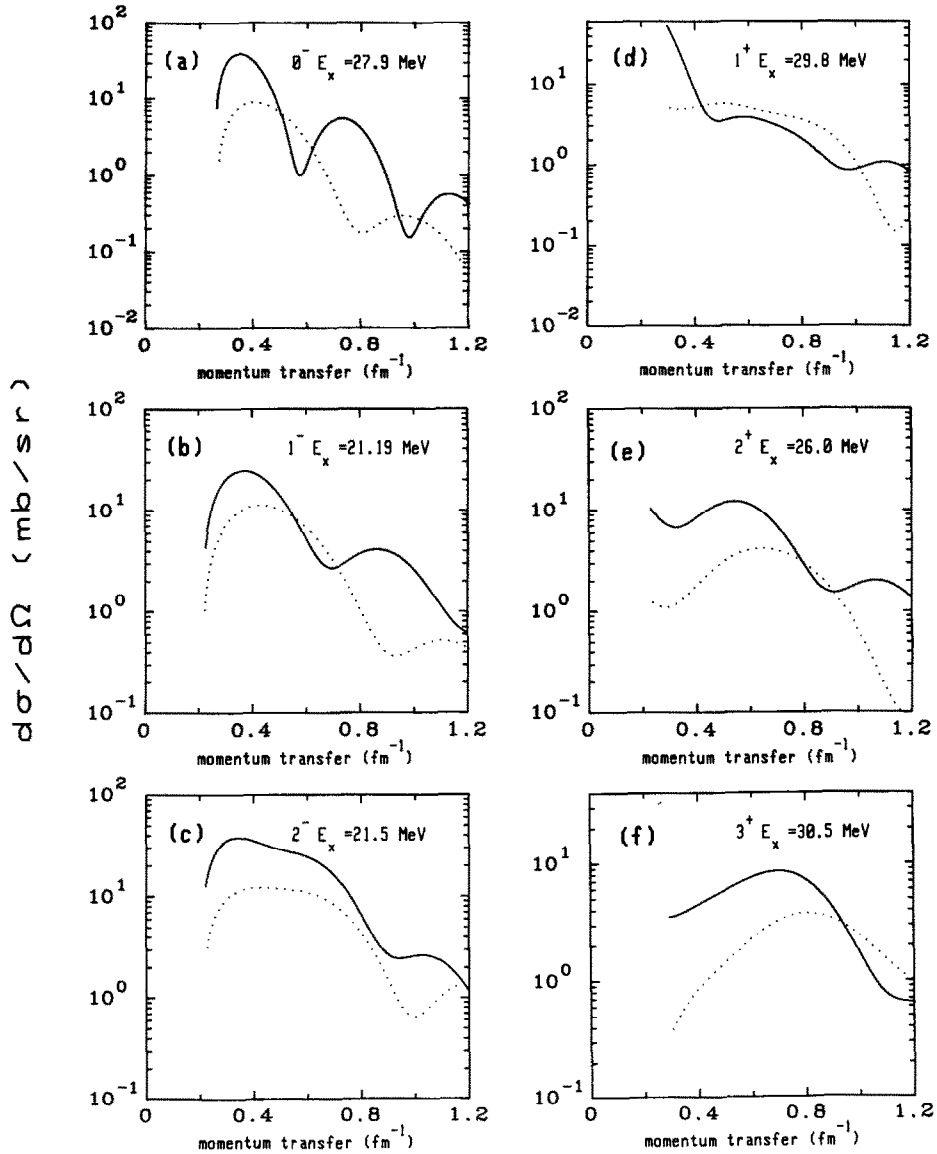


Fig. 7. Angular distributions for the $^{90}\text{Zr}(^3\text{He}, t)$ and $^{90}\text{Zr}(p, n)$ reactions leading to selected $1\hbar\omega$, $J^\pi = 0^-, 1^-, 2^-$ (figs. (a), (b), (c)) and $2\hbar\omega$, $J^\pi = 1^+, 2^+, 3^+$ (figs. (d), (e), (f)) final nucleus states in ^{90}Nb . The full curves show the $(^3\text{He}, t)$ and the dotted curves the (p, n) results. The incident energy amounts to 600 MeV in case of the $(^3\text{He}, t)$ and to 200 MeV in case of the (p, n) reactions.

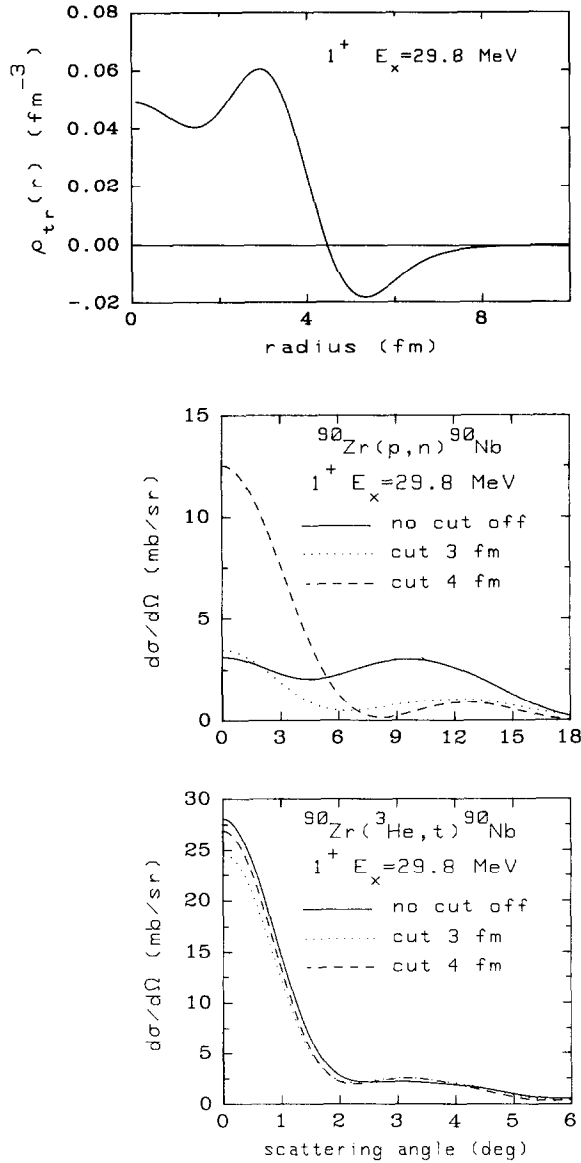


Fig. 8. Reaction mechanism study of the $^{90}\text{Zr}(^3\text{He}, t)$ and $^{90}\text{Zr}(p, n)$ reactions in case of a collective $2\hbar\omega$, $J^\pi = 1^+$ excitation. The upper part of fig. 8 shows the radial nuclear transition density to this state. The lower figures show the (p, n) and $(^3\text{He}, t)$ angular distributions for this state as a function of a lower cutoff radius R introduced in the nuclear transition form factor.

The latter corresponds to the average spreading width of the particle-hole state n . The quantities ε_F and R_w denote the Fermi energy of ^{90}Zr and the radius of the imaginary optical potential, respectively. For the optical potential W we used the energy dependent empirical proton-nucleus optical potential of Rapaport³¹⁾. The widths varied typically from 6 MeV for the GT state at $E_{\text{GT}} = 8.7$ MeV to $\Gamma = 15$ MeV for states around 20 MeV excitation energy. The asymmetry, that means the ratio $\Gamma_{n,r}/\Gamma_{n,l}$, was determined from the slope $\partial W/\partial E$ of the imaginary optical potential. We obtained $\Gamma_{n,r}/\Gamma_{n,l} \approx 2$ for states with excitation energies smaller than $E_n = 20$ MeV and $\Gamma_{n,r}/\Gamma_{n,l} = 1$ for states with $E_n \geq 20$ MeV. By the described folding procedure of the 1p1h-RPA-doorway states with the asymmetric Breit-Wigner function we effectively simulate the damping and energy shift of the states due to the coupling to 2p2h and more complicated configurations. If we compare the resultant strength distribution function with those obtained from microscopic 2p2h calculations³³⁾, we find that our procedure simulates the spreading of strength quite well.

In order to reproduce the absolute magnitude of the experimental cross sections (σ^{exp}) we introduced an overall normalization factor $N = 1.45$ in our calculated cross sections (σ^{cal}). There are two possible explanations for this discrepancy. The first is that the absolute normalization of the experimental spectrum is known only within an accuracy of 25%. The other is that the rather simple single folding procedure in determining the ^3He - and t -optical potentials might not be accurate enough. It turns out that the absolute magnitudes of the differential cross sections are sensitive to the depth of the imaginary optical potential. If we decrease, e.g., the depth of the imaginary optical potential by 27% we obtain an increase in the cross section to the GT state of 45%. This would correspond to our overall normalization factor.

In fig. 9 we present the $^{90}\text{Zr}(^3\text{He}, t)$ spectra for the scattering angles $\theta = 0^\circ$, $\theta = 2.5^\circ$ and $\theta = 4.3^\circ$. The full lines are the experimental data and the dashed curves are the calculated spectra. For comparison we also plotted our old calculations¹⁵⁾ performed in a $2\hbar\omega$ RPA model space (dotted curves).

The low energy part of the 0° ($^3\text{He}, t$) spectrum is clearly dominated by the $0\hbar\omega$, $L=0$, GT-transitions and is described well by our calculations. However, in the high energy part, i.e. in the energy range $15 \text{ MeV} \leq E_x \leq 40 \text{ MeV}$, the experimental data are underestimated by our calculations. This part of the spectrum is dominated by the $2\hbar\omega$, $L=2$, $J^\pi = 1^+$, 2^+ and 3^+ transitions. In the (p, n) reaction at $E = 200$ MeV the contributions of the $2\hbar\omega$ modes to the 0° spectra are small. The enhancement of these modes in the ($^3\text{He}, t$) spectrum can be explained by the surface character of the ($^3\text{He}, t$) reaction. We discussed this point already in the previous chapter.

The low energy part, $0 \leq E_x \leq 15 \text{ MeV}$, of the 0° ($^3\text{He}, t$) spectrum is dominated by the $0\hbar\omega$, $L=0$, GT transitions and is well described by our calculations. The high energy part ($15 \text{ MeV} \leq E_x \leq 40 \text{ MeV}$), on the other hand, is underestimated by our calculations. This part of the spectrum is dominated by the $2\hbar\omega$, $L=2$, $J^\pi = 1^+$,

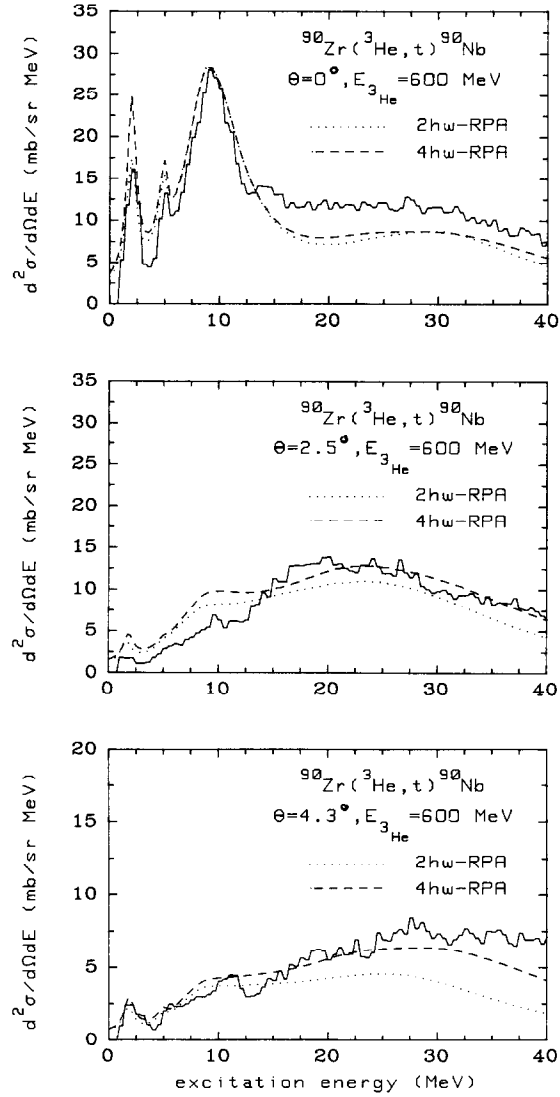


Fig. 9. Spectra for the reaction $^{90}\text{Zr}(^3\text{He}, t)$ at the bombarding energy of 200 MeV per nucleon for the scattering angles $\theta = 0^\circ$, 2.5° and 4.3° . The data (full line) are taken from refs. ^{13,14}). The dotted curves are the calculations performed in a $2\hbar\omega$ -RPA model space while the dashed curves are the results obtained in a $4\hbar\omega$ -RPA model space.

2^+ and 3^+ transitions. The reason for this underestimate is not obvious. It is certainly *not* a convergence problem of the calculations since the $2\hbar\omega$ - and $4\hbar\omega$ -model space results do not differ from each other at this scattering angle. It is interesting that we find just the opposite situation for the $\theta = 2.5^\circ$ spectrum. In this case the low energy part of the spectrum is overestimated by the calculations while the high energy part is reproduced well. In view of the fact that the $\theta = 4.3^\circ$ spectrum is described well at all excitation energies one is led to the following possible explanation for the discrepancies found between experiment and theory at the very forward scattering angles. The diffraction pattern of the differential cross sections might not be correct because the single folding procedure used for generating the optical potentials in the incident and exit channels is not accurate enough. Especially the radius of the imaginary optical potential could be too small leading, for example, to a too slow fall off of the GT angular distribution with angle. Then the GT cross section at scattering angles $\theta \geq 0^\circ$ will be too large.

From the $\theta = 2.5^\circ$ and $\theta = 4.3^\circ$ spectra in fig. 9 it is obvious that a large RPA model space is needed to achieve convergence in the calculations. In table 1 we show the energy integrated cross sections ($E_x \leq 40$ MeV) of the different multipoles included in the calculations. It can be observed that the inclusion of states with $J^\pi \leq 5^+$, 5^- is sufficient to achieve convergence of the cross section calculations for

TABLE 1
Energy integrated cross sections (integration interval: $0 \leq E_x \leq 40$ MeV) of states with different final spins J^π at scattering angles $\theta = 0^\circ$, 2.5° and 4.3° ^{a)}

	Energy integrated strength (≤ 40 MeV)		
	0.0°	2.5°	4.3°
EXP	487.4	335.7	205.2
TOT	435.3	370.2	188.8
GT	237.2	29.9	9.6
0^+	11.8	0.7	0.8
1^+	289.8	46.5	13.7
2^+	27.6	43.4	13.7
3^+	40.4	63.8	41.1
4^+	1.5	4.1	8.2
5^+	1.1	2.8	3.8
0^-	11.3	11.3	6.3
1^-	9.6	49.2	10.0
2^-	26.2	104.2	38.9
3^-	7.4	21.4	29.1
4^-	8.3	22.0	21.6
5^-	0.4	1.0	1.9

^{a)} The energy integrated total experimental and theoretical cross sections are denoted by EXP and TOT, respectively. GT is the summed Gamow-Teller cross section of the low ($E_x = 2.3$ MeV) and high ($E_x = 8.7$ MeV) lying GT-states.

scattering angles $\theta \leq 4.3^\circ$. Furthermore one sees from the table that we underestimate the energy integrated experimental cross section for the scattering angles $\theta = 0^\circ$ and $\theta = 4.3^\circ$ by about 10% but that we overestimate the cross section at $\theta = 2.5^\circ$ by about 10%. An interesting feature is that the GT states cover only about 55% of the total cross section at $\theta = 0^\circ$. From the analysis of the (p, n) spectra we know that the GT states contribute 74% to the spectrum at $\theta = 0^\circ$. This clearly indicates that the higher multipoles are much stronger excited at $\theta = 0^\circ$ in the (^3He , t) reactions than in the (p, n) reactions. Note that at $\theta = 0^\circ$ there is an appreciable amount of $2\hbar\omega$ strength with multipolarities $J^\pi = 1^+$, 2^+ and 3^+ . Especially the $2\hbar\omega$, $J^\pi = 1^+$ transitions contribute 52 mb to the spectrum.

4. Concluding remarks

Within the framework of the distorted wave impulse approximation (DWIA) we presented a new method for the microscopic calculation of inelastic and charge exchange scatterings induced by composite particles. For the first time both the direct and knock-on exchange amplitudes are included in the calculations exactly. In order to carry out the calculations we used the multipole expansion method which is repeatedly applied in performing the multidimensional integrals involved in the transition amplitudes. In the limit of a point projectile size the basic formulae for the composite particle scattering reduce to those of nucleon-nucleus scattering.

A computer code (DCP1) was developed which includes the knock-on exchange amplitudes exactly. This code was then applied to examine the NR approximation which is often used in calculating the exchange effects. We found that the NR approximation generally overestimates the exact cross sections by 10–50%. We also studied the tensor exchange effects and found that the tensor exchange amplitudes are very small and can be safely neglected in the calculations. The cross sections of the (^3He , t) reaction are very sensitive to both central and tensor forces. This is very similar to what one knows from the analysis of the (p, n) reaction.

After these reaction mechanism studies we presented a microscopic calculation of the forward angle $^{90}\text{Zr}(^3\text{He}, \text{t})$ spectrum at 600 MeV incident energy. The nuclear structure calculations were performed in a $4\hbar\omega$ model space. All states with multipolarities $J^\pi \leq 5^-$ were included in the analysis of the data. We found that the experimental spectra up to 40 MeV excitation energy can be very well described by direct one step processes only. That means that the measured spectra can be interpreted as the linear spin-isospin response of the nucleus to the probing (^3He , t) field.

In contrast to the $^{90}\text{Zr}(\text{p}, \text{n})$ reaction we found that the “background” with respect to the GT states is strongly enhanced in the (^3He , t) reaction. This enhancement can be understood as arising from a stronger excitation of the $2\hbar\omega$, $L = 2$ transitions in this reaction than in the (p, n) reaction. The reason for this behaviour is the strong surface character of the (^3He , t) reaction.

In order to reproduce the high energy tail of the spectrum we performed the nuclear structure calculations in a $4\hbar\omega$ model space. We still underestimate the 0° spectrum above 25 MeV but we can now reproduce the experimental data at higher scattering angles very well up to excitation energies ≤ 40 MeV.

In summary, we have shown that the $(^3\text{He}, t)$ reaction is a very useful tool to study spin-isospin correlations in nuclei.

One of the authors (T.U.) wishes to express his sincere thanks to Professor J. Speth for his kind hospitality extended to him during his stay at KFA Jülich, where the major part of this work was done. This work was partially supported by the US Department of energy.

References

- 1) R.R. Doering *et al.*, Phys. Rev. Lett. **35** (1975) 1961
- 2) D.E. Bainum *et al.*, Phys. Rev. Lett. **44** (1980) 1751
- 3) C.D. Goodman *et al.*, Phys. Rev. Lett. **44** (1980) 1775
- 4) D.J. Horen *et al.*, Phys. Lett. **95B** (1980) 29; **99B** (1981) 383
- 5) C. Gaarde *et al.*, Nucl. Phys. **A369** (1981) 258
- 6) F. Osterfeld, Phys. Rev. **C26** (1982) 762
- 7) T. Izumoto, Nucl. Phys. **A395** (1983) 183
- 8) F. Osterfeld and A. Schulte, Phys. Lett. **138B** (1984) 23
- 9) F. Osterfeld, D. Cha and J. Speth, Phys. Rev. **C31** (1985) 372
- 10) A. Klein, W.G. Love and N. Auerbach, Phys. Rev. **C31** (1985) 710
- 11) J. Bang *et al.*, Nucl. Phys. **A440** (1985) 445
- 12) M. Yabe, F. Osterfeld and D. Cha, Phys. Lett. **192B** (1987) 26
- 13) C. Ellegaard *et al.*, Phys. Rev. Lett. **50** (1983) 1745 and also private communication with C. Gaarde
- 14) C. Gaarde, Proc. Int. Conf. on nuclear physics Harrogate UK 25-30 August 1986
- 15) A. Schulte, T. Udagawa, F. Osterfeld and D. Cha, Phys. Lett. **183B** (1987) 243
- 16) R. Schaeffer and J. Raynal, unpublished
- 17) F. Osterfeld, Code FROST-MARS, unpublished
- 18) M. Igarashi, Code TWOFNR, unpublished
- 19) W.G. Love and G.R. Satchler, Nucl. Phys. **A159** (1970) 1;
W.G. Love and L.W. Owen, Nucl. Phys. **A239** (1975) 74
- 20) T. Udagawa, A. Schulte and F. Osterfeld, to be published
- 21) R. Schaeffer, Nucl. Phys. **A158** (1970) 321
- 22) T. Kammuri, Nucl. Phys. **A263** (1976) 178
- 23) F. Petrovich and D. Stanley, Nucl. Phys. **A275** (1977) 487
- 24) J. Bang *et al.*, Nucl. Phys. **A429** (1984) 330
- 25) P.J.A. Buttle and L.J.B. Goldfarb, Nucl. Phys. **78** (1966) 409;
T. Sawaguri and W. Tobocman, J. Math. Phys. (N.Y.) **6** (1967) 1855
- 26) F. Petrovich *et al.*, Phys. Rev. Lett. **22** (1969) 895
- 27) G.R. Satchler, Direct nuclear reactions (Clarendon, Oxford, 1983)
- 28) M. Yabe, A. Schulte, T. Udagawa and F. Osterfeld, to be published
- 29) J. Wambach, F. Osterfeld, J. Speth and V.A. Madsen, Nucl. Phys. **A324** (1979) 77
- 30) W.G. Love and M.A. Franey, Phys. Rev. **C24** (1981) 1073
- 31) J. Rapaport *et al.* Nucl. Phys. **A296** (1978) 85
- 32) I.S. McCarthy, I. Sick and R.R. Whitney, Phys. Rev. **C15** (1977) 1396
- 33) S. Drozd, F. Osterfeld, J. Wambach and J. Speth, Phys. Lett. **189B** (1987) 271
- 34) G.M. Crawley *et al.*, Phys. Rev. **C26** (1982) 87